Katabatic Flow Mechanisms on a Low-Angle Slope

THOMAS HAIDEN

Zentralanstalt für Meteorologie und Geodynamik, Vienna, Austria

C. DAVID WHITEMAN

Pacific Northwest National Laboratory, Richland, Washington

(Manuscript received 13 October 2003, in final form 30 June 2004)

ABSTRACT

Momentum and heat budget equations for katabatic flows on sloping surfaces are revisited. Terms in these equations are evaluated using wind and potential temperature data from four tethered-balloon data collection systems on a 3-km line running down a 1.6° slope at the foot of the Oquirrh Mountains in Utah's Great Salt Lake valley. The analyses focus on the development with downslope distance of the katabatic flow and the associated negatively buoyant layer under synoptically undisturbed conditions. With strong ambient stratification, the katabatic flow shows little variation between sites, suggesting a state close to local equilibrium. When the ambient stratification is weaker, the acceleration of the katabatic flow between two tethersonde sites is systematically larger than what would be predicted based on observed buoyancy. Comparison of observed flow direction with the local topographic gradient indicates that slope curvature, associated with small deviations from the basically planar slope, may be responsible for the anomalous increase. It is concluded that the cross-slope homogeneity of the flow, which is assumed in simplified katabatic flow models, may be significantly disturbed even on slopes that appear to be planar to the observer.

1. Introduction

The apparent simplicity of the katabatic flow mechanism, namely, denser air flowing downhill because of gravity, has prompted the design of many simplified models. Early work by Prandtl (1942) demonstrated how the basic characteristics of katabatic flows could be modeled analytically by assuming local equilibria in the heat and momentum budgets, and constant turbulent diffusivities. Starting with the work of Fleagle (1950), another type of simplification, the bulk (or hydraulic) model, was introduced. In contrast to Prandtl's analysis, which was based on the concept of local equilibrium and focused on vertical profiles, hydraulic katabatic flow models were designed to predict the along-slope evolution of vertically integrated flow characteristics. The bulk approach was elaborated on and extended by Ball (1956), Manins and Sawford (1979a), Fitzjarrald (1984), and Kondo and Sato (1988), among others. In these models a balance of two to three dominant terms in the momentum and heat budget equations was assumed to keep the problem analytically tractable. With regard to the momentum equation, Mahrt (1982) provided a rigorous scale analysis and critical evaluation of approximations used by different authors.

The rationale behind hydraulic slope flow modeling is that for some practical applications like dispersion modeling, or the parameterization of subgrid-scale transports in NWP and climate models, a good estimation of bulk mass flux values would be valuable even if the details of the slope wind profile are not known. For example, the subsiding motion induced in a valley or basin atmosphere by slope flows is determined by their bulk mass flux. The physical assumption underlying hydraulic slope flow modeling is that bulk variables, such as mass flux, momentum flux, or bulk buoyancy deficit, can be related to each other through a closed system of equations without explicit reference to details in the vertical profiles. It implies that katabatic flows exhibit a certain degree of similarity in the temperature and wind profiles, which can be expressed mathematically in the form of nondimensional shape factors (Manins and Sawford 1979a).

Corresponding author address: Thomas Haiden, Central Institute for Meteorology and Geodynamics, Hohe Warte 38, A-1190 Vienna, Austria.
E-mail: thomas.haiden@zamg.ac.at

Hydraulic katabatic flow models make specific, testable predictions about the along-slope evolution of bulk temperature deficit, flow strength, and flow depth. Up to now there has been limited direct verification of such along-flow variations. A comparison of observed and predicted relationships between flow depth and slope length over a wide range of slopes of different lengths and inclinations was presented by Kondo and Sato (1988). Their analysis shows, on average, an increase of flow depth with slope length in the observations, in agreement with hydraulic model predictions. On the other hand it also shows deviations from the average behavior, which will require further explanation. Doran et al. (1990) compared the sign of observed along-slope variations of temperature deficit, inversion strength, and inversion depth with the predictions of the Manins and Sawford (1979a) model. For a simple slope on the side of an isolated mountain they found better agreement than for a slope on a valley sidewall, but even on the simple slope systematic differences were noted. For example, the observed inversion strength remained roughly constant along the slope, whereas a decrease was predicted by the model because of entrainment.

What makes direct verification of simplified katabatic flow models difficult is that they are usually based on the assumption of negligible ambient wind, an exception being the theoretical work of Fitzjarrald (1984). Thus, the models should be verified only against observations in which the katabatic flow speed significantly exceeds the ambient wind speed. Typical observed bulk katabatic flow speeds are in the range of 2–3 m s^{-1} on slopes of length 1 km or longer and are on the order of 1 m s^{-1} on slopes with lengths of a few hundred meters (Mahrt 1982; Doran et al. 1990). Thus, a synoptic wind of 1–2 m s^{-1} would already be too strong to allow a clear interpretation of observed katabatic flows in terms of simplified models. The practical difficulty in separating the katabatic flow component from the background flow was also noted by Doran and Horst (1983). The purpose of this paper is to gain further understanding of bulk katabatic flow characteristics by comparing new observational data obtained during the U.S. Department of Energy's Vertical Transport and Mixing (VTMX) experiment (Doran et al. 2002) with predictions of simplified models. The experimental site, consisting of an array of four tethersondes that are aligned west–east, corresponding to the general topographic gradient in the area, is briefly described in section 2. Even though the inclination angle of the slope is rather small (1.6°), strong katabatic flows were observed, with maximum downslope speeds exceeding 5 m s^{-1}. A short description of observed flow and inversion characteristics is given in section 3. Budget equations for momentum and heat are formulated in section 4, and individual terms in the budgets as estimated from the tethersonde measurements are presented in section 5. It is shown that the comparison with the hydraulic model results suggests the presence of strong slope curvature effects, which are discussed in section 6.

2. Data

a. Site and experimental setup

The data used in this paper come from a set of meteorological experiments conducted in October 2000 in the Great Salt Lake valley (also called the Jordan River valley) on a low-angle slope on the valley floor 28 km south-southwest of Salt Lake City at the foot of the Oquirrh Mountains (Fig. 1). This slope was selected because of its uniform angle, homogeneous surface and topographic characteristics, altitude, and accessibility. The smooth slope was formed by wave action on the shoreline of glacial Lake Bonneville, an extensive ice age lake that covered much of the Salt Lake valley (the Great Salt Lake is the present-day remnant of glacial Lake Bonneville). The slope has no major tributaries cutting through it and has few small-scale drainage channels, although on a scale of 500 m or so it exhibits a weak rolling topography (Fig. 2). The slope was strip cropped so that the surface was covered with alternating fields of disked soil (fallow land) and wheat stubble. The slope's altitude range is within the normal range of temperature inversion depths in the Salt Lake valley (Jackman 1968), ensuring that regular diurnal changes in static stability occur over the slope as the valley temperature inversion builds up in the evening and breaks up following sunrise. October temperature inversions, as observed at the Salt Lake City airport 28 km north of the slope, are typically 3.9°C over a depth of 295 m (Jackman 1968). The slope is accessible from nearby roads and from dirt tracks made in the wheat stubble. The slope on which the experiments were conducted had a uniform inclination angle of 1.6° and was located approximately 4–7 km east of the foot of the waste rock pile at Kennecott Utah Copper's Bingham Canyon (an open-pit copper mine).

Apart from having rather small inclination, the slope studied here differs from the ones previously investigated in that it is located at the foot of steeper topography with a complicated, three-dimensional structure. This makes the slope representative of a large number of valley–floor slopes in alpine-type areas, but also raises the question of upstream influence. Our primary objective is to understand flow variations on the simple slope itself. Thus, we regard the flow and temperature structure at the uppermost site as given, and test whether bulk models can predict katabatic flow conditions at the other sites downstream.

The design of the slope experiments and details regarding the meteorological equipment and sites were presented by Whiteman et al. (2002) and will not be repeated here. The main observational equipment was a set of four tethered balloon sounding systems ar-

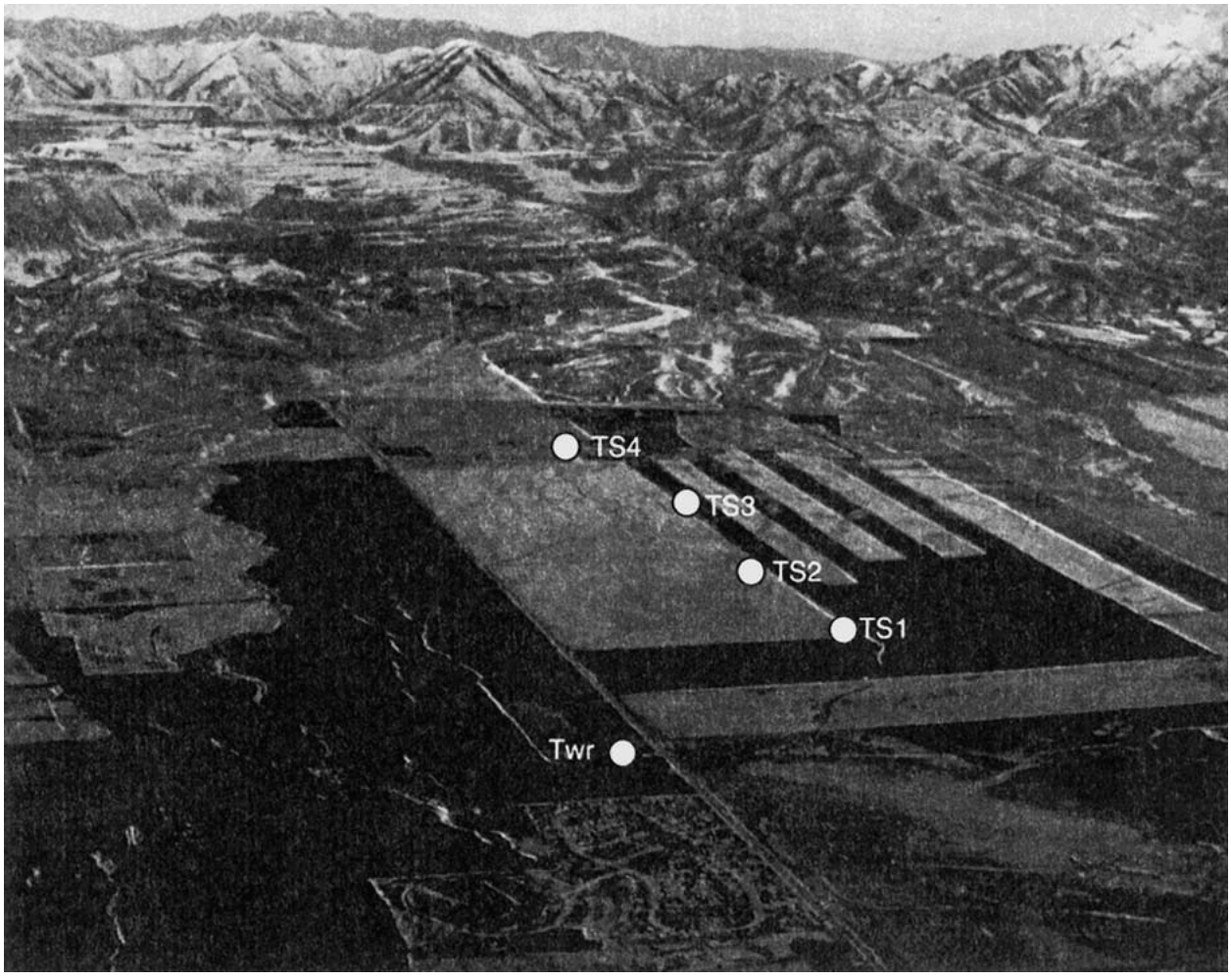

FIG. 1. Oblique aerial photograph of the slope site in Nov 2001 showing the approximate locations of the tethersonde sites. In Oct 2000, when the experiments were conducted, the surface cover on the slopes was reversed (fallow land was replaced by wheat stubble, and vice versa).

ranged on a line running down the slope and separated by about 1 km each (Figs. 2 and 3). The line began about 3.5 km below the Kennecott waste pile. For ease in referring to the individual tethered balloon systems, the sites are designated as TS1, TS2, TS3, and TS4 (numbered from the lowest to the highest altitudes of 1485, 1513, 1539, and 1572 m MSL, respectively).

The tethered balloon sounding systems made synchronous coordinated ascents to heights of 200–300 m AGL at roughly half-hourly intervals. The tethersonde at TS1 occasionally made deeper ascents to approximately 450 m to investigate the valley atmosphere above the slope boundary layer. After the ascents, the balloons were retrieved quickly and the sondes were allowed to equilibrate at the ground before their next ascents. Downsoundings were discarded and have not been used in the analyses. The sondes measured temperature, relative humidity, pressure, wind speed, and wind direction. Pre- and postexperiment calibrations were performed on the tethersondes and the data were corrected for the minor differences noted. Other meteorological instruments in addition to the tethersondes were operated on the slope. Data reported in this paper come from a sonic anemometer (9.1 m AGL) and a scintillometer (2.6 m AGL over a beam length of 180 m).

Experiments were conducted during the intensive observational periods (IOPs) declared by investigators of the Department of Energy's VTMX experiment (Doran et al. 2002). These 21-h IOPs began at 1500 mountain standard time (MST). The data used in this paper come from selected individual ascents made during the evenings of IOP1, IOP4, and IOP5 on 2, 8, and 14 October 2000, respectively, when skies were clear, upper winds were weak, and katabatic flows were well developed on the slope. Tethersonde TS4 was not operating during IOP1, which makes TS3 the uppermost site in the budget analysis in that case.

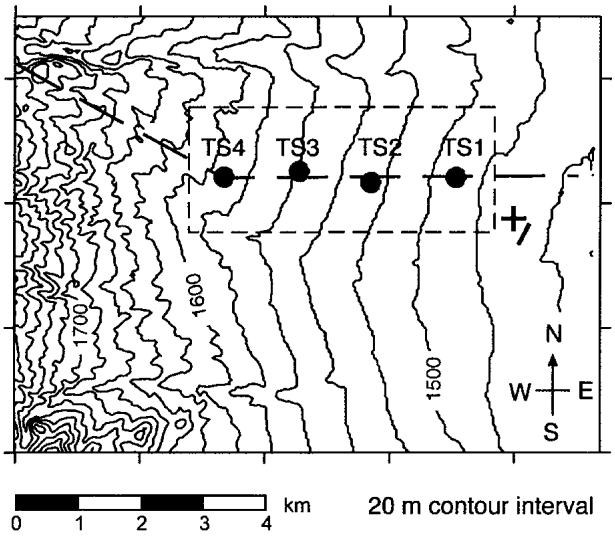

FIG. 2. Contour map of the slope area, showing the locations of the four tethersondes TS1–TS4 (filled circles), the slope tower on which the sonic anemometer was deployed (+), and the scintillometer path (short, thick line near tower). The thick dashed line indicates the cross section of Fig. 3. The dashed rectangle shows the domain used in the topographic curvature calculations (cf. Fig. 9).

b. Data selection

In order to identify the primary flow mechanisms we aimed at systematically selecting the most undisturbed soundings. Visual inspection of the data showed pronounced katabatic flows during IOP1, IOP4, and IOP5. Tethersonde soundings taken during those IOPs were subjected to an objective ranking scheme based on the ratio of the downslope wind speed at the height of the jet maximum to the ambient wind speed. Ambient wind speed was defined as the minimum speed above the slope flow layer. It was usually found in the height range between 80 and 150 m AGL. A ratio ≥ 3, averaged over the tethersonde profiles TS1–TS3, was defined as a necessary condition for the wind field to be dominated by katabatic flow. This criterion was met in seven cases, which form the basis of this study. Table 1 shows some flow characteristics of these cases, and the ambient stability during the three IOPs.

In order to obtain robust estimates of vertically nonintegrated quantities, such as the height of the jet maximum, or the depth of the katabatic layer, small-scale inhomogeneities in the vertical profiles of wind and temperature had to be smoothed. To this end, a three-point running average operator was run repeatedly over the profiles. Also, the ranking scheme described above was applied to the smoothed profiles. Vertically integrated quantities were computed from the original, unsmoothed profiles (such as those shown in Figs. 4–6).

3. Observed flow characteristics

Figures 4 and 6 illustrate basic features of the flow that were observed under conditions of weak ambient stability such as were present during IOP1 and IOP5 (cf. Table 1). Despite the rather small terrain inclination, the katabatic flow shows a well-developed jet profile, with speeds up to 7 m s^{-1} in the case of IOP1, and 5–6 m s^{-1} in the case of IOP5. There is a pronounced surface inversion with temperature deficits reaching 8 and 5 K in IOP1 and IOP5, respectively. The stronger inversion and higher jet speeds in the IOP1 profiles, as compared with the IOP5 profiles, is mostly due to the different time of day (2130 vs 1907 MST). The 1916 MST profiles from IOP1, which were not included here because they ranked too low, show a jet of 5–6 m s^{-1}, and a surface inversion of about 5 K, just like the IOP5 profiles from 1907 MST. The vertical extent of significant downslope flow ranges between 50 and 100 m, whereas the vertical extent of the cold air is approximately half of this value. Above the surface inversion, the difference in temperature at the different sites is generally less than 1 K, which suggests that the theoretical concept of an undisturbed, horizontally homogeneous basic-state temperature field is appropriate. The downslope wind speed does not drop to zero above

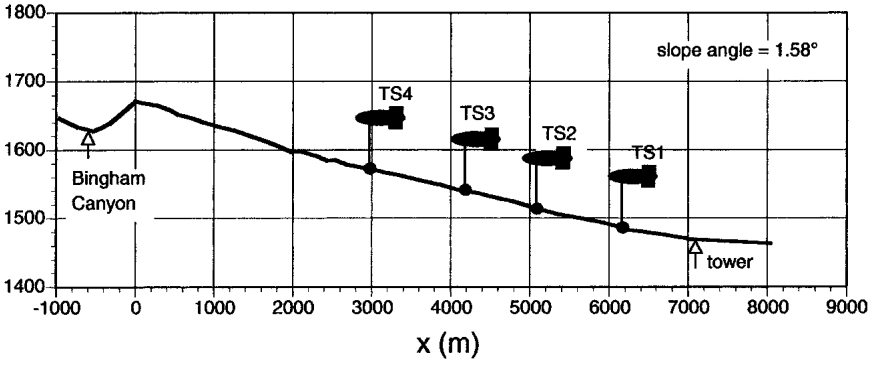

FIG. 3. Topographic cross section of the slope along the dashed line in Fig. 2 showing the location of the tethersonde sites and the tower.

TABLE 1. List of katabatic flow cases selected by the ranking scheme (index values ≥ 3).

IOP No.	Date	Time (MST)	Ambient wind speed (m s^{-1})	Jet speed (m s^{-1})	Jet height (m)	Ranking index	Ambient stability (K m^{-1})
1	2 Oct 2000	1954	0.6	5.3	18	11.3	0.0025
		2101	0.7	4.7	16	6.9	
		2130	1.3	5.9	13	4.6	
4	8 Oct 2000	1855	1.3	3.7	8	3.0	0.0010
		1924	0.7	3.7	8	5.4	
5	14 Oct 2000	1907	1.2	4.0	14	3.2	0.0025
		1930	1.1	3.7	13	3.4	

the katabatic flow, but reaches an average value of 0.5–1.5 m s^{-1}, which is small, but not negligible, in comparison with the katabatic flow speeds. In the formulation of the momentum budget (section 4), this is taken into account. The downslope wind speed generally increases along the slope, in particular, between TS3 and TS2. The magnitude of the surface inversion shows a weak tendency of along-slope increase.

Figure 5 shows the profiles for a case from IOP4, when ambient stability was roughly 4 times as high (cf. Table 1). Both katabatic flow speed and inversion strength are smaller than during IOP1, but the basic characteristics of the profiles are similar. In contrast to IOP1 and IOP5, the wind speed does not increase from TS3 onward, but appears to have reached some kind of equilibrium profile. All katabatic flow cases selected by the ranking procedure were observed during early night. After midnight, flow conditions typically became more disturbed due to the development of a larger-scale down-valley (i.e., cross slope) flow. A more comprehensive description of observed flow characteristics is given by Whiteman et al. (2002).

4. Budget equations for momentum and heat

Hydraulic katabatic flow models are based on simplified versions of the bulk momentum equation and, depending on the model, the bulk heat equation. They differ with regard to the choice of terms retained. In order to obtain a clear picture of the simplifications involved and a general frame of reference, we first derive the complete budget equations. We use a two-dimensional, rotated, orthogonal coordinate system in which the x axis coincides with the slope, and the z axis is perpendicular to the slope. Following the notation of Mahrt (1982), any dependent variable ϕ^* is partitioned into a horizontally homogeneous basic state at rest ϕ_0, a time-averaged perturbation ϕ, and a turbulent fluctuation ϕ'. In order to deal with positive quantities, we orient the x axis such that it points in the *downslope* direction, and we define θ as the temperature *deficit*. Because the vertical scale of the katabatic flow is generally much smaller than the scale height of the atmosphere, the Boussinesq approximation for shallow flows can be applied. Coriolis effects are neglected as we consider flow variations over a horizontal scale of 1–10 km, corresponding to Rossby numbers $>>1$. We make the usual boundary layer approximations in which turbulent flux divergences are neglected in the w equation of motion, and generally in the x direction. The resulting set of equations governing conservation of momentum, heat, and mass can be written as

$$\frac{\partial u}{\partial t} + u\frac{\partial u}{\partial x} + w\frac{\partial u}{\partial z} = -\frac{1}{\rho_0}\frac{\partial p}{\partial x} + g\frac{\theta}{\theta_0}\sin\alpha - \frac{\partial \tau}{\partial z}, \quad (1)$$

$$\frac{\partial w}{\partial t} + u\frac{\partial w}{\partial x} + w\frac{\partial w}{\partial z} = -\frac{1}{\rho_0}\frac{\partial p}{\partial z} - g\frac{\theta}{\theta_0}\cos\alpha, \quad (2)$$

$$\frac{\partial \theta}{\partial t} + u\frac{\partial \theta}{\partial x} + w\frac{\partial \theta}{\partial z} = -\gamma(u\sin\alpha - w\cos\alpha) - \frac{\partial F}{\partial z}, \quad (3)$$

and

$$\frac{\partial u}{\partial x} + \frac{\partial w}{\partial z} = 0, \quad (4)$$

where α is the slope angle, γ is the vertical gradient of the basic-state potential temperature, $\tau = \overline{u'w'}$ and $F = \overline{w'\theta'}$ are the turbulent fluxes of u and θ in the direction perpendicular to the slope, and otherwise standard notation is used. Because of the rotated coordinate system, buoyancy terms appear both in (1) and (2), and advection of the basic-state potential temperature field in (3) involves both velocity components. Direct longwave cooling of the air by radiative flux divergence is neglected. A linearized version of (1)–(4) was used by Egger (1981) in his theoretical study on two-dimensional slope wind circulations. If along-slope variations are neglected, and turbulent transport terms are parameterized using the K theory with constant turbulent diffusivities, we obtain the well-known Prandtl (1942) model of thermally driven slope flow. It is usually assumed that the slope normal velocity component is small compared to the along-slope component, which means (2) reduces to an expression of hydrostatic equilibrium between perturbation temperature and perturbation pressure in the direction normal to the slope, that is,

$$-\frac{1}{\rho_0}\frac{\partial p}{\partial z} = g\frac{\theta}{\theta_0}\cos\alpha. \quad (5)$$

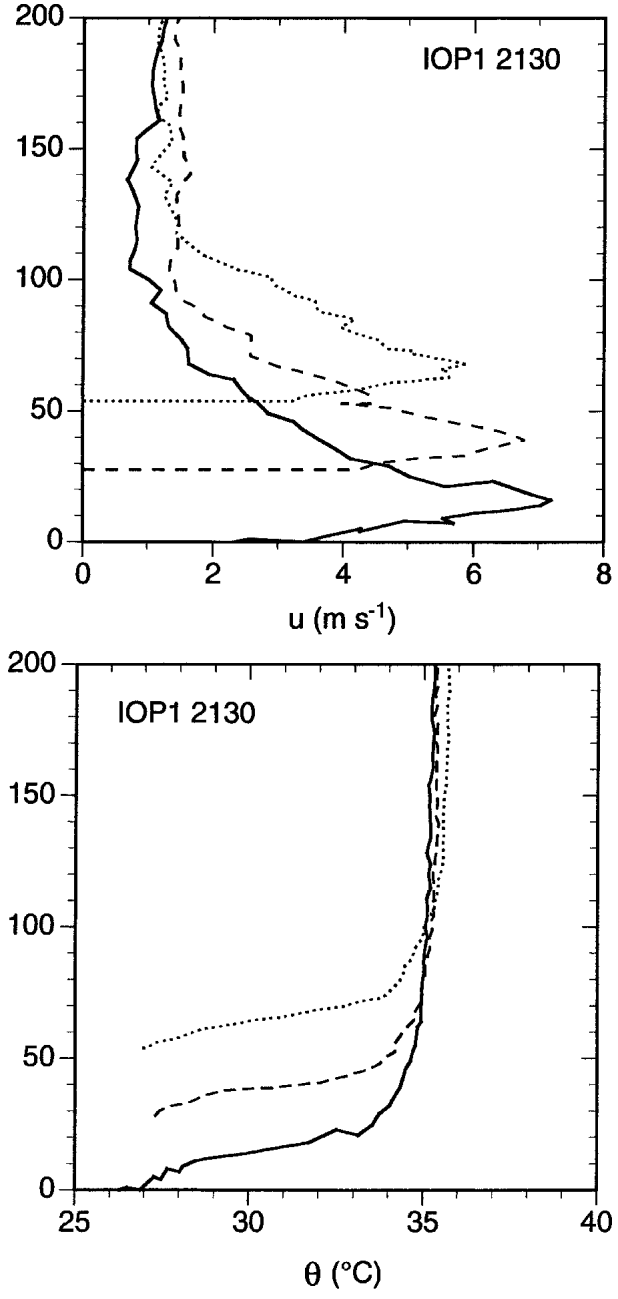

FIG. 4. Vertical profiles of (top) downslope wind speed and (bottom) potential temperature at tethersonde sites TS1 (solid), TS2 (dashed), and TS3 (dotted) during IOP1 at 2130 MST (TS4 was not operating during IOP1). The vertical axis indicates height above the surface at the lowermost site (TS1).

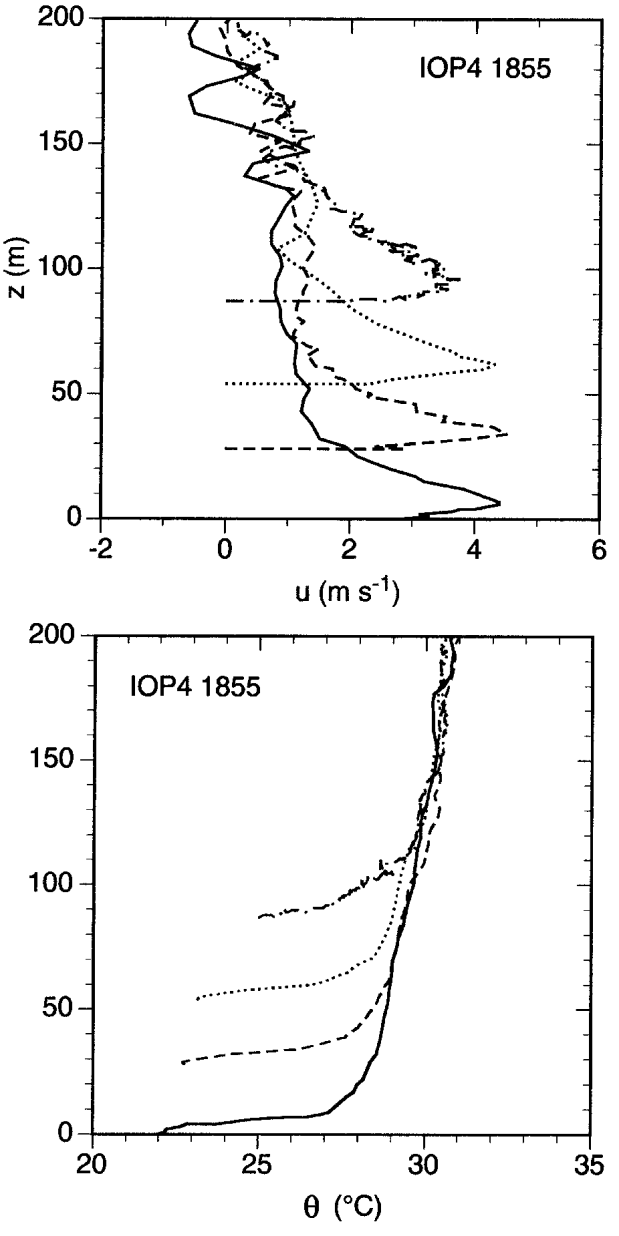

FIG. 5. As in Fig. 4, vertical profiles of (top) downslope wind speed and (bottom) potential temperature at tethersonde sites TS1–TS4 during IOP4 at 1855 MST. The vertical axis indicates height above the surface at the lowermost site (TS1). TS4 is the dashed–dotted curve.

By integrating (5) in the z direction, the pressure gradient term in the u momentum equation can then be expressed in terms of perturbation potential temperature as

$$\frac{1}{\rho_0}\frac{\partial p}{\partial x}(z) = \cos\alpha \frac{g}{\theta_0}\frac{\partial}{\partial x}\int_z^h \theta(z')\, dz', \qquad (6)$$

where h is a level above the katabatic flow layer where the temperature perturbation is negligibly small. While the assumption of small w considerably simplifies the problem it is strictly applicable only on slopes that are sufficiently homogeneous and extended. In other words, the along-slope length scale over which significant flow variations occur must be much larger than the depth of the katabatic flow layer (Mahrt 1982; Haiden 2003).

Bulk equations for downslope momentum and heat

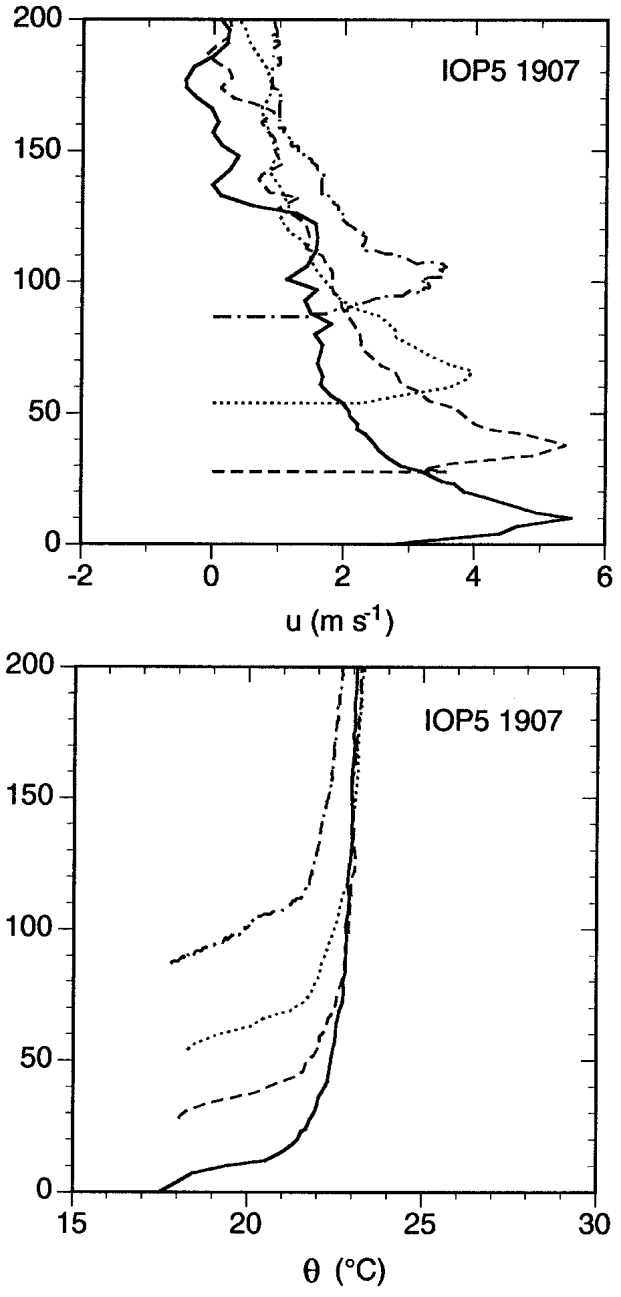

FIG. 6. As in Fig. 5, vertical profiles of downslope (top) wind speed and (bottom) potential temperature at tethersonde sites TS1–TS4 during IOP5 at 1907 MST. The vertical axis indicates height above the surface at the lowermost site (TS1).

can be derived by layer integrating (1) and (3) from $z = 0$ to $z = h$, using (4) and (6). As pointed out by Fitzjarrald (1984), the form of the resulting equations depends on whether h defines an undisturbed reference level that is constant in space and time, or the actual top of the katabatic layer. Here we use the method of constant h, for which layer integration of (1) and (3) gives

$$\frac{\partial}{\partial t} h\bar{u} + \frac{\partial}{\partial x} h\overline{u^2} = \frac{g}{\theta_0} h\bar{\theta} \sin\alpha - \frac{g}{\theta_0} \cos\alpha \frac{\partial}{\partial x} h^2 \bar{\bar{\theta}} - w_h u_h + \tau_0 - \tau_h \quad \text{and} \tag{7}$$

$$\frac{\partial}{\partial t} h\bar{\theta} + \frac{\partial}{\partial x} h\overline{u\theta} = -\gamma h(\bar{u} \sin\alpha - \bar{w} \cos\alpha) - w_h \theta_h + F_0 - F_h, \tag{8}$$

where

$$\bar{\phi} = \frac{1}{h} \int_0^h \phi(z)\, dz \quad \text{and}$$

$$\bar{\bar{\phi}} = \frac{1}{h^2} \int_0^h \int_z^h \phi(z')\, dz'\, dz.$$

The terms on the rhs of the bulk momentum equation [(7)] are buoyancy, the thermal wind term, kinematic entrainment (detrainment) of momentum due to the mean flow, and turbulent stress divergence across the layer. The terms on the rhs of the bulk temperature equation [(8)] are advection of the background temperature field, kinematic entrainment (detrainment) of perturbation temperature, and turbulent temperature flux divergence. Simplified versions of (7) and (8) form the basis of bulk models of katabatic flow. For the momentum equation, a systematic analysis of simplifying assumptions underlying various models was presented by Mahrt (1982). Manins and Sawford (1979a) introduced empirical, dimensionless shape coefficients to relate the product of two bulk quantities to the bulk quantity of the product, for example, $\bar{u}\bar{\theta}$ to $\overline{u\theta}$. Mahrt (1982) provided stationary solutions to this equation under the assumption of constant flow depth, and with the stress divergence term parameterized as

$$\tau_0 - \tau_h = -(C_D + k)\overline{u^2}, \tag{9}$$

where C_D is the surface drag coefficient, and k represents frictional forces due to momentum exchange at the interface between the katabatic flow and the ambient atmosphere. A number of authors (e.g., Ball 1956; Businger and Rao 1965; Petkovsek and Hocevar 1971; Manins and Sawford 1979a; Kondo and Sato 1988) derived simplified solutions to (7) and (8) by considering a reduced set of terms in the equations.

As stated in the introduction, we restrict our analysis to differences between sites. Thus, for the actual evaluation of terms using observational data we need to integrate (7) and (8) over a finite distance along the slope. The finite-distance increment and the mean value of a quantity ϕ between two points x_0 and $x_0 + L$ are denoted by

$$\Delta(\phi) = \phi(x_0 + L) - \phi(x_0) \quad \text{and}$$

$$[\phi] = \frac{1}{L} \int_{x_0}^{x_0+L} \phi(x)\, dx, \tag{10}$$

respectively. With these definitions, the resulting budget equations take the forms

$$\underbrace{Lh\frac{\partial}{\partial t}[\overline{u}]}_{\text{U\_STOR}} + \underbrace{\Delta(h\overline{u^2})}_{\text{U\_ADV}} = \underbrace{Lh\frac{g}{\theta_0}[\overline{\theta}]\sin\alpha}_{\text{BUOY}} \underbrace{- \frac{g}{\theta_0}\cos\alpha\Delta(h^2\,\overline{\overline{\theta}})}_{\text{THERM}} \underbrace{- L[w_h u_h]}_{\text{U\_ENTR}} + \underbrace{L[\tau_0 - \tau_h]}_{\text{FRIC}} \quad \text{and} \tag{11}$$

$$\underbrace{Lh\frac{\partial}{\partial t}[\overline{\theta}]}_{\text{T\_STOR}} + \underbrace{\Delta(h\overline{u\theta})}_{\text{T\_ADV}} = \underbrace{-\gamma Lh([\overline{u}]\sin\alpha - [\overline{w}]\cos\alpha)}_{\text{T\_MEAN\_ADV}} \underbrace{- L[w_h\theta_h]}_{\text{T\_ENTR}} + \underbrace{L[F_0 - F_h]}_{\text{DIAB}}. \tag{12}$$

In the subsequent budget analysis the abbreviations given below (11) and (12) will be used to reference individual terms. They can also be used to characterize different simplified models that have been proposed in the literature. Some are based only on the momentum equation and assume a simple two-term balance, for example, U_ADV = BUOY, which was termed advective gravity flow by Mahrt (1982), or BUOY + FRIC = 0, corresponding to a slope flow that is in local dynamic equilibrium (Kondo and Sato 1988). Note that the term FRIC contains both surface friction and turbulent entrainment, whereas kinematic entrainment of momentum is denoted by U_ENTR. This term is often neglected, but we evaluate it in the budget analysis taking into account the nonnegligible ambient wind speeds that were observed. Similarly, the effects of turbulent and kinematic entrainment on the heat budget are contained in DIAB and T_ENTR, respectively. The model used by Manins and Sawford (1979a) corresponds to U_ADV = BUOY + THERM + FRIC, and T_ADV = T_MEAN_ADV + DIAB.

5. Momentum and heat budgets

The available measurements do not permit evaluation of all terms in the budget equations with equal precision. For example, the friction and diabatic cooling terms (FRIC, DIAB) can only be estimated indirectly and are, therefore, much more uncertain than BUOY or T_MEAN_ADV. For the thermal wind term THERM and the storage terms U_STOR and T_STOR, the situation is regarded as intermediate because their evaluation is a direct one, but involves space and time differences.

The determination of the upper limit of integration h was based on the wind speed profile. Visual inspection of the profiles revealed a broad minimum, typically at a height between 80 and 150 m AGL, of both the downslope wind component u and the wind speed $V = \sqrt{u^2 + v^2}$. The lower boundary of the layer of low wind speed was determined quasi objectively using an algorithm that starts at the level of strongest negative shear above the jet and searches upward until the shear in either u or V drops below a certain threshold, which was set to 0.005 s^{-1}. The resulting values of h found from individual ascents were then averaged within IOPs, giving 131, 82, and 115 m for IOP1, IOP4, and IOP5, respectively.

In the derivation of (6) we stated that h represents a height where the temperature perturbation is negligibly small. This does not have to be the lowest height at which it is negligibly small. If there is a layer of finite thickness on top of the katabatic flow layer in which there is no temperature perturbation, then the integrand on the right-hand side of (6) will give no contribution in that layer. Consequently, the result of the integration will be insensitive to the exact choice of h. The same is true for the bulk fluxes of momentum and heat. As long as the integrated quantities themselves are considered, rather than their means obtained through division by h, the sensitivity to the exact value of h is small provided that h is located sufficiently high for perturbation quantities to be small. However, in the derivation of (8) and subsequent budget equations, one must decide whether h is taken as constant along the slope or is not. This is because in the latter case additional terms appear because of the horizontal and time derivatives of the upper limit of integration. We chose a constant h for each IOP to avoid such additional terms. Although this implies a compromise between individual soundings, we minimize the sensitivity of our results to the exact value of h by choosing a height close to the wind speed minimum. This is also true for the heat budget because in most cases the temperature perturbation at the height of the windspeed minimum is negligibly small (see Figs. 4–6).

The temperature deficit θ at a given site and level was determined as the difference between a background temperature at that height and the observed temperature. A linear background temperature profile is estimated for each IOP from a superposition of the upper, quasi-linear segments of the tethersonde ascents that, when overlaid on an absolute height diagram, nearly coincide (cf. Figs. 4–6). The background potential temperature gradients found by this method were 2.5 K km^{-1} for IOP1 and IOP5 and 10 K km^{-1} for IOP4 (see also Table 1).

The continuous lines in Figs. 7 and 8 show observed along-slope variations of the bulk momentum flux $h\overline{u^2}$ and bulk heat flux $h\overline{u\theta}$, respectively. The momentum flux generally increases along the slope in the less stable IOP1 and IOP5 and assumes a nearly constant value in

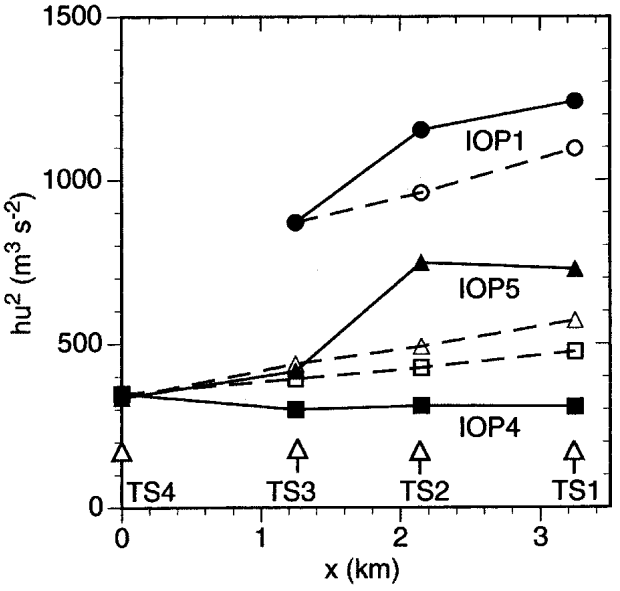

FIG. 7. Observed downslope evolution of bulk momentum flux (solid lines). For comparison, the dashed lines show the theoretical evolution due to buoyancy alone, corresponding to advective gravity flow.

the more stable IOP4. Figure 7 also shows the theoretical evolution of momentum flux, assuming that the observed buoyancy is the only force driving the flow in addition to the momentum advection. This corresponds to the "advective gravity" model, where only the terms

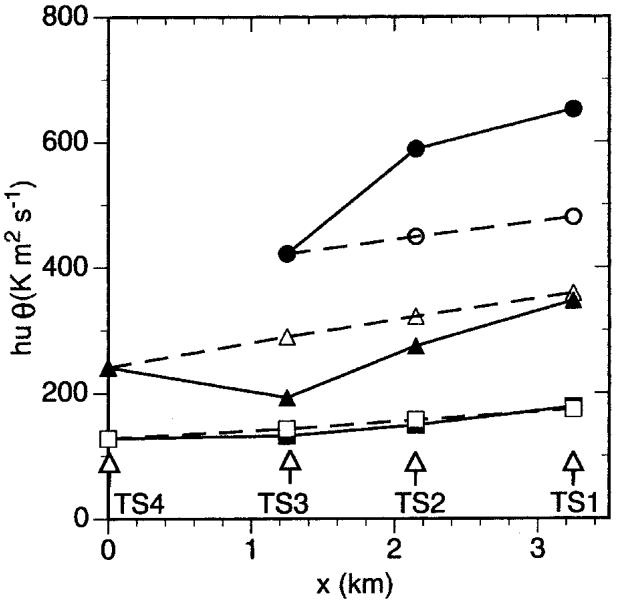

FIG. 8. Observed downslope evolution of bulk temperature deficit flux (solid lines). For comparison, the dashed lines show the corresponding theoretical evolution for a sensible heat flux divergence of 55 W m^{-2}, taking into account along-slope advection of the background temperature field.

U_ADV and BUOY are retained in (11). It can be seen that during the two less stable IOPs the observed momentum flux increase along the slope exceeds the theoretical values by a large amount, in particular, between TS3 and TS2. A stronger-than-expected increase between TS3 and TS2 is found also for the bulk flux of the temperature deficit (Fig. 8). As in the case of momentum, we take the prediction of a simple model, in this case "advective diabatic," as a reference. The dashed lines show the theoretical increase of $h\overline{u\theta}$ based on an assumed sensible heat flux divergence (SHFD) of 55 W m^{-2}, assuming stationary flow and taking into account advection of the background temperature field. This corresponds to assuming a three-term balance between T_ADV, T_MEAN_ADV, and DIAB in (12). The SHFD of 55 W m^{-2} was chosen such that it approximately matched the observed downslope evolution of bulk temperature deficit during IOP4, which appears to be the one closest to local equilibrium. Using the same value of SHFD as a reference for the other IOPs we find, as in the case of momentum, an observed increase of heat flux from TS3 to TS2 that significantly exceeds theoretical predictions. It is important to note that this conclusion is valid for the entire range of physically plausible SHFD values, including those estimated from sonic anemometer and scintillometer measurements made close to the tethersonde sites. In fact one would have to assume an unrealistically large SHFD of more than 100 W m^{-2} across the katabatic flow layer to reproduce the observed increase of $h\overline{u\theta}$ along the slope.

Several of the terms in the budget equations [(11) and (12)] can be roughly estimated from the tethersonde data. The spatial finite difference operator in (10) is evaluated exactly by taking differences between sites, and the average operator in (10) is approximated by the arithmetic mean. To obtain results less sensitive to short-term fluctuations, the vertical profiles of individual ascents within a given IOP for a given site are averaged, representing time periods of 1.5 h in the case of IOP1, and 0.5 h for IOP4 and IOP5 (cf. Table 1). The time derivatives on the lhs of the budget equations are approximated by finite differences between the last and first ascent within each time period. Terms difficult to quantify are the turbulent momentum and heat flux divergences FRIC and DIAB. If the various terms are evaluated in this manner, indirect estimation of DIAB based on the SHFD necessary to maintain the katabatic flow during IOP4 suggests a value close to 35 W m^{-2}. This is smaller than the 55 W m^{-2} derived under the stationarity assumption because of the decrease with time of the bulk temperature deficit in the katabatic flow layer during IOP4 (negative T_STOR in Table 3). Measurements obtained from a scintillometer (mean height 2.6 m AGL over a beam length of 180 m) and sonic anemometer at 9.1 m AGL suggest a downward sensible heat flux around 15 W m^{-2} during early nighttime. This is significantly less than one would expect

under clear, dry conditions, when net radiation is on the order of 70–80 W m^{-2}. If it is assumed that the ground heat flux approximately compensates one-half of the net radiative loss, then a crude "climatological" estimate for DIAB would be in agreement with the value of 35 W m^{-2} derived from the IOP4 budget. The same value was applied to the other two IOPs, and the uncertainty inherent in this estimation must be considered when interpreting the budget. The turbulent momentum flux divergence FRIC is estimated using (9), with a value of $C_D + k = 0.01$ for the total drag coefficient. This value corresponds to what Mahrt (1982) found to be a likely upper limit.

Table 2 gives the results for the momentum budget. Momentum storage U_STOR is found to be either weak or negative, which means the strength of the flow decreases with time. The along-slope increase of momentum flux U_ADV attains very large values between TS3 and TS2, leading to large positive residuals. The thermal wind term THERM gives a small or negative contribution to the momentum budget (with the exception of TS4→TS3 during IOP5), due to a general increase of bulk temperature deficit along the slope. Kinematic entrainment of momentum (U_ENTR) is significant only when the along-slope mass flux increase is large, which coincides with those cases where the along-slope momentum flux increases strongly (TS3→TS2 during IOP1 and IOP5).

The budget for along-slope variations in the flux of temperature deficit is shown in Table 3. As in the case of momentum, large imbalances are found in IOP1 and IOP5. The along-slope increase of the flux of temperature deficit (T_ADV) is so large that it can not be explained by the combined effect of diabatic cooling and storage (DIAB, T_ADV). Basic-state advection T_MEAN_ADV always gives a negative contribution (warming) in a stable atmosphere. Kinematic entrainment of temperature deficit (T_ENTR) into the katabatic layer is completely negligible because the integration height is far above the top of the cold air.

In summary, the budgets are far from closed during IOP1 and IOP5. Some additional large forcing terms must be present to produce the observed increase of momentum flux between TS3 and TS2, and the increase of the flux of temperature deficit between the two sites. This conclusion is not sensitive to the uncertainty involved in the estimation of the turbulent surface fluxes. Apart from Coriolis and nonhydrostatic pressure forces, which can both be assumed to be small by scaling arguments, all terms in the derivation of the budget equations were taken into account. Thus, we are forced to question the only remaining assumption, which is the two-dimensionality of the flow or, in other words, the assumption of homogeneity in cross-slope direction. This has important implications for our ability to verify simplified slope flow models using point observations of real katabatic flows. For the budget analysis it means that we must take a closer look at the topography itself and identify possible causes of persistent cross-slope variations of the katabatic flow.

TABLE 2. Individual terms in the along-slope evolution of the bulk flux of momentum (m^3 s^{-2}). Residuals give the amount of additional forcing that would be needed on the rhs of (11) to balance the lhs.

	Term in (11)	TS4 → TS3	TS3 → TS2	TS2 → TS1
IOP1	U_STOR		−1	−5
	U_ADV		283	87
	BUOY		90	135
	THERM		−59	−22
	U_ENTR		30	3
	FRIC		−70	−101
	Residual		291	67
IOP4	U_STOR	−27	−31	−30
	U_ADV	−48	11	−3
	BUOY	46	33	49
	THERM	−9	7	−23
	U_ENTR	−17	2	1
	FRIC	−49	−34	−41
	Residual	−46	−28	−18
IOP5	U_STOR	−23	−23	−32
	U_ADV	81	332	−20
	BUOY	103	52	80
	THERM	107	9	−38
	U_ENTR	9	49	−2
	FRIC	−41	−46	−71
	Residual	−120	267	−21

TABLE 3. Individual terms in the along-slope evolution of the bulk flux of temperature deficit (K m^2 s^{-1}). Residuals give the amount of additional forcing that would be needed on the rhs of (12) to balance the lhs.

	Term in (12)	TS4 → TS3	TS3 → TS2	TS2 → TS1
IOP1	T_STOR		1	5
	T_ADV		167	63
	T_MEAN_ADV		−19	−25
	T_ENTR		0	0
	DIAB		30	36
	Residual		157	57
IOP4	T_STOR	−20	−26	−24
	T_ADV	5	16	29
	T_MEAN_ADV	−49	−33	−41
	T_ENTR	0	0	0
	DIAB	41	30	36
	Residual	−7	−7	9
IOP5	T_STOR	−18	3	17
	T_ADV	−48	82	72
	T_MEAN_ADV	−16	−14	−20
	T_ENTR	0	0	0
	DIAB	41	30	36
	Residual	−91	70	82

6. Slope curvature

Most natural slopes are not planar but possess curvature, causing the height contours to deviate from straight lines. Consequently, if the katabatic flow ap-

proximately follows the topographic gradient, there will be patterns of confluence and diffluence. In a two-dimensional analysis, bulk momentum and heat fluxes (vertically integrated but per unit width) will increase and decrease along the slope, due to this effect. As a first step beyond the two-dimensional framework we consider a flow that is still homogeneous in the cross-flow direction but exhibits confluence and diffluence, analogous to a flow in a channel of varying width (Manins and Sawford 1979b). In this case the advective terms on the lhs of (7) and (8) must be replaced by

$$\frac{1}{a}\frac{\partial}{\partial x}\,ah\overline{u^2} = \frac{\partial}{\partial x}\,h\overline{u^2} + h\overline{u^2}\,\frac{1}{a}\frac{da}{dx} \quad \text{and} \tag{13}$$

$$\frac{1}{a}\frac{\partial}{\partial x}\,ah\overline{u\theta} = \frac{\partial}{\partial x}\,h\overline{u\theta} + h\overline{u\theta}\,\frac{1}{a}\frac{da}{dx} \tag{14}$$

to allow conservation of momentum and heat between streamlines that are a varying distance $a(x)$ apart. If we assume that the flow roughly follows the topographic gradient then in the infinitesimal limit $(1/a)(da/dx)$ becomes the topographic curvature r^{-1}. This produces the following additional terms on the right-hand side of the bulk momentum and heat budgets (7) and (8)

$$\left(\frac{\partial}{\partial x}\,h\overline{u^2}\right)_{\text{CURV}} = -\frac{h\overline{u^2}}{r} \quad \text{and} \tag{15}$$

$$\left(\frac{\partial}{\partial x}\,h\overline{u\theta}\right)_{\text{CURV}} = \frac{h\overline{u\theta}}{r}. \tag{16}$$

In areas of convex topography (diffluence, $r > 0$) it gives a negative contribution, while in areas of concave topography (confluence, $r < 0$) a positive contribution is given. We are using the word confluence rather than convergence because a lateral contraction (dilatation) of streamlines along the flow does not necessarily entail significant vertical motion. It could be accompanied by longitudinal acceleration (deceleration), with little vertical motion, especially when static stability is large. In the hypothetical case of constant curvature acting as the only forcing term, (15) and (16) would give an exponential along-flow increase (decrease) of bulk fluxes with the radius of curvature r as the e-folding distance.

For a given two-dimensional topography $z_s(x, y)$ the local curvature is given by the convergence of the normalized topographic gradient

$$\frac{1}{r} = -\nabla \cdot \left(\frac{\nabla z_s}{|\nabla z_s|}\right). \tag{17}$$

Because of the second-order differential the values obtained from (17) for real topography on a discrete grid will be very sensitive to grid resolution. Curvature is generally ill defined when the topographic surface exhibits fractal-like characteristics. In such cases increasing the resolution of the digital elevation data will produce strongly increasing values of curvature. However, r^{-1} as used in (15) and (16) represents not the topographic curvature as such but that of an "equivalent" topography that corresponds to the degree of smoothness of the bulk katabatic flow vector field. It is important to bear in mind that on real slopes even the simple notion of "downslope direction" may be ambiguous and resolution dependent. Figure 2 shows that the downslope direction of the slope considered here is more or less easterly on the scale of 5-km resolution. Resolved on a scale of 1 km, the downslope direction becomes approximately east-southeast in the area of the tethersonde array. On an even smaller scale (100 m) we find more complicated structures, such as an east-northeast orientation of the slope just south of site TS2, and east-southeast just north of it (Fig. 9).

At different heights above the terrain katabatic flows will follow different topographic gradients. In their observational study, Manins and Sawford (1979b) noted the presence of a "skin flow" a few meters deep that differed in flow direction from the bulk of the katabatic flow above. Similarly, Mahrt et al. (2001) observed near-surface drainage flows of up to a 3-m depth following a shallow gully of ~100-m width. Above, the katabatic flow direction was oriented with the larger-scale slope in which the gully was embedded. An important practical question is which direction the bulk mass flux vector will take. To obtain a definitive answer based on observations, a two-dimensional array of tethersondes would be needed. However, some limited information can be gained from the one-dimensional array used here, if combined with a high-resolution topographic gradient vector field.

Elevations in a limited area (marked by the dashed rectangle in Fig. 2) surrounding the tethersonde array were digitized by hand onto a grid with 100 m × 100 m resolution from a detailed topographic map of the U.S. Geological Survey (USGS; 1:24000 Lark, Utah, contour interval 20 ft). Visual linear interpolation between isolines was used to assess the elevation at individual grid points. We estimate that the procedure was accurate to within ±2 m. Comparison between contour plots from the digitized dataset and the USGS map confirmed that topographic features of size 200–300 m and larger were accurately resolved, and no spurious surface irregularities were introduced by the method. From the elevation data the normalized negative topographic gradient $-\nabla z_s/|\nabla z_s|$ and slope curvature, as defined by (17), were computed. Figure 9c shows the resulting vector field and curvature patterns. It can be seen that the slope exhibits significant variation in slope angle and orientation on the 100-m scale. Apparently, on low-angle slopes even moderately large *relative* variations in slope inclination (say, 50%) are hard to discern visually by the in situ observer because the corresponding *absolute* variations of inclination are small (see also Fig. 1). However, in terms of katabatic flow dynamics a 50% change of inclination means a 50% change in forcing no matter how small the slope angle.

Observed bulk flow vectors at the tethersonde sites,

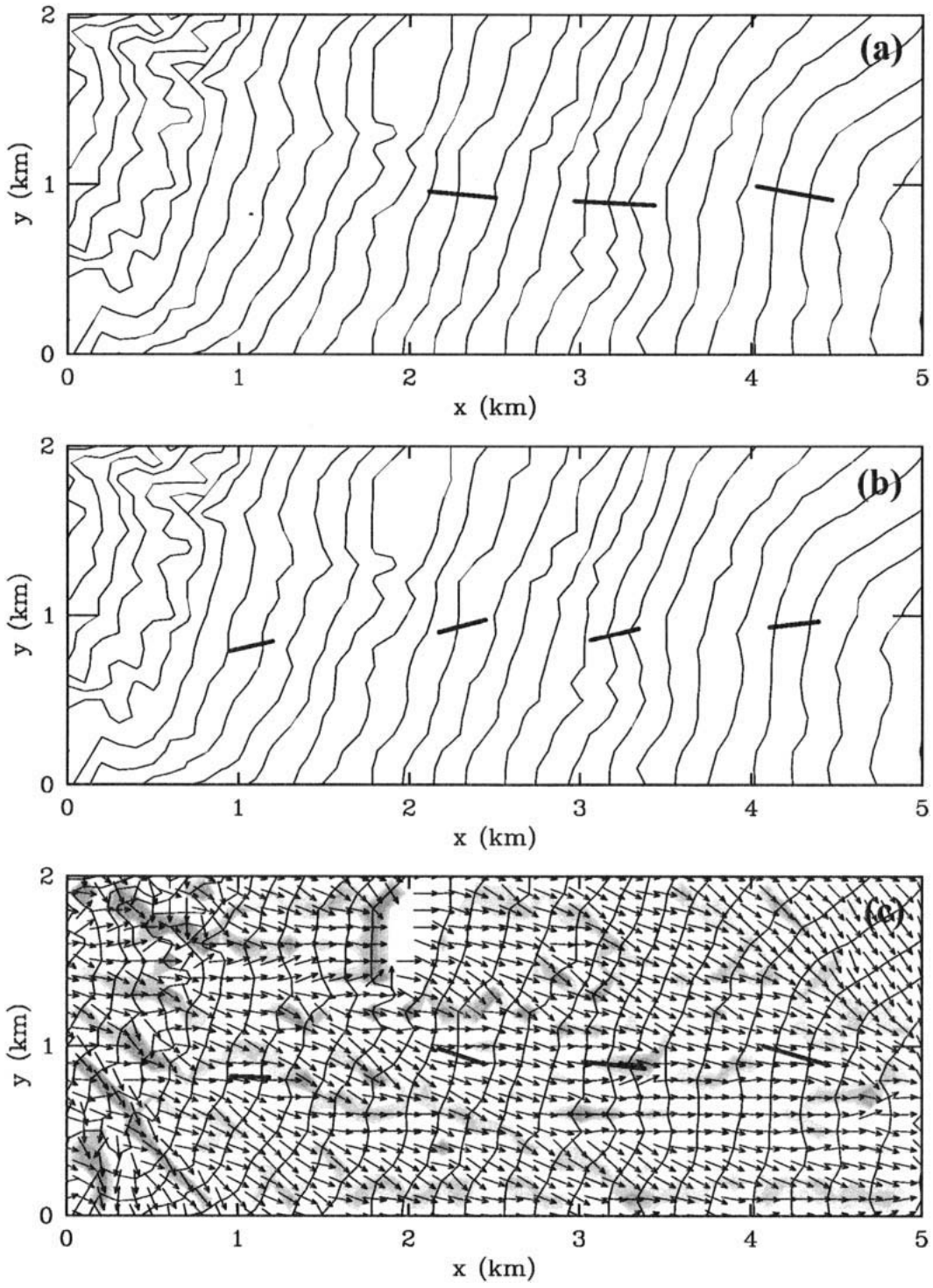

FIG. 9. Slope topography at a horizontal resolution of 100 m (contour interval 10 m), and mean observed flow direction and strength in the katabatic layer during (a) IOP1 at 2130 MST, (b) IOP4 at 1855 MST, and (c) IOP5 at 1907 MST at tethersonde sites TS4–TS1, from left to right, respectively (short thick lines). Note that TS4 was not operating during IOP1. The bottom panel also shows the normalized negative topographic gradient (vector field). Shading indicates amount of concave slope curvature computed using (17). The darkest shading indicates curvature values on the order of 0.01 m^{-1}, corresponding to the resolution of 100 m of the topographic dataset.

averaged over the lowest 20 m, are indicated in Figs. 9a–c by short bold lines. In the case of IOP5 (Fig. 9c) there is fairly good agreement between observed flow directions and the topographic gradient at the four sites. It appears that the more westerly flow at sites TS4 and TS2, as compared with the more northwesterly flow at TS3 and TS1, is related to local slope orientations at those sites. Figure 9a shows that a slightly stronger northerly component of TS3 and TS1, as compared with TS2, is also present in IOP1 (TS4 was not operating during this IOP), although the variation in bulk flow direction between sites is only a few degrees in this case. Tethersonde site TS2, which has shown an unexpectedly large bulk momentum and heat fluxes in the budgets of IOP1 and IOP5, is located in an area of pronounced concave topography. At the resolution of 100 m used, the negative curvature reaches values up to $r^{-1} = -0.007\ \mathrm{m}^{-1}$ there. The average curvature along a straight path from TS3 to TS2 is about $-0.0004\ \mathrm{m}^{-1}$, which gives a roughly 40% increase of bulk fluxes between the two sites. It is an effect of sufficiently large magnitude to explain the increase of momentum and heat flux between TS3 and TS2 (cf. Figs. 7 and 8) and the magnitude of the residuals in the budgets (cf. Tables 2 and 3). In principle, one could integrate slope curvature along streamlines to evaluate (15) and (16) as additional terms in the budget, but as Fig. 9c shows the results will be extremely sensitive to the exact choice of the integration path. Also, because of this path dependence it is not certain that the air sampled at one tethersonde site is representative of the air that flows past the next site downstream, as is implicitly assumed in a two-dimensional approach. A fully three-dimensional flow model run at very high resolution with a higher-order turbulence closure would be necessary to obtain a more detailed quantitative analysis of the confluence effect and its role in the budgets.

During IOP4 the observed bulk flow vectors had a larger southerly flow component and did not follow the local topographic gradient (Fig. 9b). A comparison with Fig. 9c shows that this implies quite different paths and curvature "histories" along individual streamlines. The more southerly flow appears to be linked to a trough that was approaching from the west, although the exact mechanism remains uncertain. Doran et al. (2002) reported on a downward penetration of southerly winds from aloft late in IOP4. In the earlier period studied here (1855 and 1924 MST), however, a direct downward mixing of southerly momentum is not supported by the tethersonde data, which shows that the southerly component was only 100 m deep.

The distinct flow direction patterns shown in Fig. 9 generally persisted for consecutive ascents within each IOP. One exception is the IOP1 ascent from 1954 MST, which was made shortly before an ~1/2-h disturbed period in which the westerly katabatic flow changed to northwesterly (2033 MST, not shown) and back to westerly (2101 MST). It is not clear whether such fluctuations are related to drainage flows originating in the complex topography surrounding the slope site, similar to the ones observed on the east side of the Great Salt Lake valley by Monti et al. (2002), or caused by internal flow dynamics on the slope itself.

The topographic gradient on the 1-km scale is oriented toward an azimuth of approximately 290°, differing by about 20° from the orientation of the tethersonde array, which is close to 270°. However, the corresponding underestimation of terrain inclination and, consequently, of the buoyancy forcing computed in the momentum budget, amounts to only ~6% [$1 - \cos(20°)$]. It is, thus, smaller by at least one order of magnitude than the missing forcing attributed to curvature effects.

7. Conclusions

This study has analyzed along-slope variations of bulk momentum and heat fluxes in katabatic flow observed on a low-angle slope during synoptically undisturbed conditions. The flow is characterized by maximum jet speeds of 4–5 m s^{-1} at a height of 8–15 m above ground. Vertically integrated budget equations for momentum and heat were used to identify the dominant forcing terms in comparison with what is usually assumed in simplified models. Under conditions of strong ambient stratification (IOP4) the observed flow speed shows little systematic variation in the along-slope direction. In the bulk momentum budget, buoyancy is basically balanced by friction. In the bulk heat budget, surface cooling is nearly balanced by advection of the background temperature field. Thus, the flow is close to the state of local equilibrium that is assumed in the classical Prandtl model. Under conditions of weaker stratification (IOP1 and IOP5) there is a strong along-slope increase of the fluxes of downslope momentum and heat deficit, with only a slight deepening of the katabatic flow layer. This increase is mainly due to higher flow speeds at the lower tethersonde sites. Evaluation of individual terms in the momentum budget shows that the amount of increase found in the momentum flux between locations TS3 and TS2 cannot be explained in a two-dimensional framework. Likewise, the increase of the flux of heat deficit significantly exceeds the estimated diabatic cooling between the two locations. Based on the budget analysis it is conjectured that local flow confluence due to slope curvature is causing the seemingly anomalous along-slope flux increases. It is found that small-scale irregularities in the basically planar slope that are hardly visible to the in situ observer amount to significant relative inclination changes. A comparison of the topographic gradient vector field computed at a high resolution (100 m) with observed bulk flow directions during IOP5, and to a lesser degree IOP1, lends some support to the suggested curvature effect. During IOP4, which does not exhibit anomalous along-slope flux increases, flow di-

rections deviate from the local topographic gradient. An important practical consequence is that predictions by simplified models of along-slope flow variations should not be verified using point observations. Rather, volume-averaged measurements, such as those provided by remote sensing technology, should be used for this purpose.

Acknowledgments. Kennecott Utah Copper (Larry Trimble and Steve Schnoor) and their leaseholder, Dave Bastian, provided site permissions and other assistance. Matt Krmpatich from Williams Gas Pipeline West and John Hayes from the South Valley Water Reclamation District also provided site access and power. Al Astling and Fred Banes (Dugway Proving Ground) provided and operated a tethersonde, a weather station, and a radar profiler. Rich Coulter (Argonne National Laboratory) operated the minisodar and scintillometer. Chris Doran [Pacific Northwest National Laboratory (PNNL)] operated the sonic anemometer. These investigators shared their processed data following the experiment. Main tethersonde operators included Roland Mayr (University of Innsbruck), Johanna Whiteman, Robert Grandy (Utah Department of Air Quality), Xindi Bian (PNNL), Shiyuan Zhong (PNNL), James Stalker (Los Alamos National Laboratory), and Greg Poulos (Colorado Research Associates, Inc.). Many others, including Jerry Allwine (PNNL), Stephan deWekker (University of British Columbia), and students from the University of Utah, helped to operate the tethersondes or helped to install or operate equipment. The project was supported by DOE's Office of Biological and Environmental Research Environmental Meteorology Program at Pacific Northwest National Laboratory. PNNL is operated for DOE by Battelle Memorial Institute.

REFERENCES

Ball, F. K., 1956: The theory of strong katabatic winds. *Aust. J. Phys.,* **9,** 373–386.

Businger, J. A., and K. R. Rao, 1965: The formation of drainage wind on a snow-dome. *J. Glaciol.,* **4,** 833–841.

Doran, J. C., and T. W. Horst, 1983: Observations and models of simple nocturnal slope flows. *J. Atmos. Sci.,* **40,** 708–717.

——, ——, and C. D. Whiteman, 1990: The development and structure of nocturnal slope winds in a simple valley. *Bound.-Layer Meteor.,* **52,** 41–68.

——, J. D. Fast, and J. Horel, 2002: The VTMX 2000 Campaign. *Bull. Amer. Meteor. Soc.,* **83,** 1233–1247.

Egger, J., 1981: On the linear two-dimensional theory of thermally induced slope winds. *Contrib. Atmos. Phys.,* **54,** 465–481.

Fitzjarrald, D. R., 1984: Katabatic wind in opposing flow. *J. Atmos. Sci.,* **41,** 1143–1158.

Fleagle, R. G., 1950: A theory of air drainage. *J. Meteor.,* **7,** 227–232.

Haiden, T., 2003: On the pressure field in the slope wind layer. *J. Atmos. Sci.,* **60,** 1632–1635.

Jackman, D. N., 1968: A study of meteorological effect on air pollution in the Salt Lake Valley. M.S. thesis, Dept. of Meteorology, University of Utah, 80 pp.

Kondo, J., and T. Sato, 1988: A simple model of drainage flow on a slope. *Bound.-Layer Meteor.,* **43,** 103–123.

Mahrt, L., 1982: Momentum balance of gravity flows. *J. Atmos. Sci.,* **39,** 2701–2711.

——, D. Vickers, R. Nakamura, M. R. Soler, J. Sun, S. Burns, and D. H. Lenschow, 2001: Shallow drainage flows. *Bound.-Layer Meteor.,* **101,** 243–260.

Manins, P. C., and B. L. Sawford, 1979a: A model of katabatic winds. *J. Atmos. Sci.,* **36,** 619–630.

——, and ——, 1979b: Katabatic winds: A field case study. *Quart. J. Roy. Meteor. Soc.,* **105,** 1011–1025.

Monti, P., H. J. S. Fernando, M. Princevac, W. C. Chan, T. A. Kowalewski, and E. R. Pardyjak, 2002: Observations of flow and turbulence in the nocturnal boundary layer over a slope. *J. Atmos. Sci.,* **59,** 2513–2534.

Petkovsek, Z., and A. Hocevar, 1971: Night drainage winds. *Arch. Meteor. Geophys. Bioclimatol.,* **A20,** 353–360.

Prandtl, L., 1942: *Strömungslehre* (*Flow Studies*). Vieweg und Sohn, 382 pp.

Whiteman, C. D., S. Zhong, and R. Mayr, 2002: Katabatic flows on a low-angle slope in the Salt Lake Valley—Overview of the VTMX 2000 slope experiment. Preprints, *10th Conf. on Mountain Meteorology,* Park City, UT, Amer. Meteor. Soc., 6–9.